On Radiation-Based Thermal Servoing: New Models, Controls, and Experiments

Luyin Hu, David Navarro-Alarcon, *Senior Member, IEEE*, Andrea Cherubini, Mengying Li, and Lu Li

***Abstract*—In this article, we introduce a new sensor-based control method that regulates (by means of robot motion) the temperature of objects that are subject to a radiative heat source. This valuable sensorimotor capability is needed in many industrial, dermatology, and field robot applications, and it is an essential component for creating machines with advanced thermomotor intelligence. To this end, we derive a geometric-thermal-motor model, which describes the relation between the robot's active configuration and the produced dynamic thermal response. We then use the model to guide the design of two new thermal servoing controllers (one model-based and one adaptive), and analyze their stability with Lyapunov theory. To validate our method, we report a detailed experimental study with a robotic manipulator conducting autonomous thermal servoing tasks. We show that the temperature of multiple objects with unknown thermophysical properties attached to the same end-effector can be effectively regulated by controlled robot motion. Although thermal sensing is a mature technology in many industrial thermal engineering applications, its use as a feedback signal for robot control has not been sufficiently studied in the literature. To the best of our knowledge, this is the first time that temperature regulation is formulated as a motion control problem for robots.**

***Index Terms*—Adaptive control, robotic manipulation, sensor-based control, thermoception, visual servoing.**

I. Introduction

Thermal servoing is a feedback control problem that deals with the regulation of an object's temperature by means of motor actions of a rigid robot, which can either manipulate the object or the heat source. It is a frontier problem that has numerous important applications (e.g., in industrial process control, cosmetic dermatology, fire-fighting missions, etc.) where temperature needs to be dynamically controlled and the environment is uncertain. The quality, performance, and safety of these (otherwise open-loop) applications can be improved by incorporating thermal sensorimotor capabilities.

From a control systems' perspective, the automation of this type of temperature-critical tasks requires: (a) the computation of a geometric-thermal-motor (GTM) model[1] describing the relation between the robot's motion and the consequent thermal response, and (b) the development of a sensor-based strategy (that relies on the thermal interaction matrix)[2] to autonomously impose a desired heat profile onto the surface of interest. Note that unlike other perception modalities for robot control (e.g., vision [2], proximity [3], touch [4], audition [5], and even smell [6]), thermoception has not been fully formalized in the literature as a bona fide feedback signal for motion control. In the robotics community, we still lack the framework to fully exploit it. Up to now, the overwhelming use of thermoception in robotics has been to monitor processes (e.g., image-based visual servoing with thermal cameras [7]), but not to establish *explicit thermal servo-loops* [8], which are needed to accurately control temperature. Our aim in this article is to develop the necessary framework that enables the design of thermal servoing controls with radiative heat sources.

Although thermal sensing is a mature technology and has a rich history in the automation of many tasks (see, e.g., [9]–[12]), its use as a feedback signal for robot control has not been sufficiently studied in the literature [13], where only a few works have addressed this challenging servo-control problem. Some representative works that deal with explicit thermal control include: Binrui *et al.* [14], where a fuzzy controller is developed to regulate the temperature of a fuel cell actuator; Ho and Desai [15], where the influence of temperature in the deformation behavior of a surgical robot is investigated, and an explicit thermal regulator is designed; De Backer *et al.* [16], where a control method is designed to maintain a constant tool

Manuscript received July 30, 2021; accepted October 4, 2021. Date of publication November 22, 2021; date of current version June 7, 2022. This work was supported in part by the Key-Area Research and Development Program of Guangdong Province 2020 under Project 76, in part by the Research Grants Council of Hong Kong under Grant 14203917 and Grant 15212721, in part by PROCORE-France/Hong Kong Joint Research Scheme sponsored by the RGC and the Consulate General of France in Hong Kong under Grant F-PolyU503/18, in part by the Jiangsu Industrial Technology Research Institute Collaborative Funding Scheme under Grant 43-ZG9V, and in part by The Hong Kong Polytechnic University under Grant ZZHJ and Grant YBYT. *(Corresponding author: David Navarro-Alarcon.)* This article was recommended for publication by Associate Editor A. Krupa and Editor F. Chaumette upon evaluation of the reviewers' comments.

Luyin Hu, David Navarro-Alarcon, and Mengying Li are with the Department of Mechanical Engineering, The Hong Kong Polytechnic University, Hong Kong (e-mail: 19044457r@connect.polyu.hk; david.navarro-alarcon@polyu.edu.hk; mengying.li@polyu.edu.hk).

Andrea Cherubini is with the Laboratory of Informatics, Robotics and Microelectronics of Montpellier, University of Montpellier CNRS, 34090 Montpellier, France (e-mail: cherubini@lirmm.fr).

Lu Li is with the Changzhou Institute of Advanced Technology, Changzhou 213164, China (e-mail: lli@iamt.ac.cn).

This article has supplementary material provided by the authors and color versions of one or more figures available at https://doi.org/10.1109/TRO.2021.3119399.

Digital Object Identifier 10.1109/TRO.2021.3119399

[1]The GTM model is analogous to the geometric-image-motor model used in visual servoing to control the robot's motion [1]. Its derivation relies on thermophysical principles (to be introduced in Section II), which correspond to the role of a camera model in the visual servoing formulation.

[2]Similar to the interaction (Jacobian) matrix of servoing problems, a thermal interaction matrix relates the heat energy inflow/outflow toward/from the object of interest (that causes a temperature change) with the robot motion.

temperature by adjusting the spindle speed in a stir friction welding robot. However, in these types of methods, temperature control is achieved by directly modulating the power of the heat-generating components. This approach is not suitable when considering external heat sources, e.g., wildfires [17] and sunlight [18], or when the source's power should not be varied, e.g., in cosmetic procedures [19].

A different strategy is to use sensor-based control, i.e., to dynamically change the source-object geometric configuration to achieve a desired thermal response (similar to what many organisms do [20]). This can be easily done by rigid robots, since their basic function is motion control. Such approach demands the development of appropriate models that can effectively capture the system's GTM relations. This idea has been partially demonstrated in [21], where the optimal fixed location of multiple radiating heaters in a process is automatically calculated to evenly imprint a desired thermal profile onto a surface. Yet, the heater is static and the method requires exact knowledge of all thermodynamic parameters (which are generally unknown). The proposed approach has also the potential to be used, e.g., in fire-fighting [22] or volcano exploration robots [23] to calculate optimal trajectories that avoid overheating or damaging the robot's components.

The dynamic coupling between temperature and motion may seem unintuitive for humans [24], whereas many organisms extensively exploit these relations [25]. Such advanced thermoception-based behaviors can be used to solve many real-world problems (see Fig. 1). However, these advanced thermoception-based capabilities have not yet been fully incorporated in robot control, a discipline with good track record of borrowing inspiration from nature [26], but which seems to be lagging in this direction.

As a feasible solution to the aforementioned issues, in this article, we present a rigorous formulation for robot thermal servoing with radiative sources. The main contributions are as follows.

1) We develop an efficient algorithm for computing in real time the radiation-based thermal interaction matrix, which relates robot velocity and object temperature rate.
2) We present a novel robot control method for automatically regulating the temperature of grasped objects.
3) We report experiments to validate the proposed theory.

To the best of the authors' knowledge, this is the first time that temperature regulation has been formulated in the literature as a robot servoing problem. The proposed approach could advance the development of multimodal robot controllers.

The rest of this article is organized as follows. Section II presents the mathematical models. Section III derives the controller. Section IV reports results. Finally, Section V concludes this article.

II. Mathematical Modeling

A. Heat Transfer Model

Throughout this article, we denote all *column* vectors by small bold letters, e.g., $\mathbf{v} \in \mathbb{R}^{n\times 1}$, and matrices by capital bold letters, e.g., $\mathbf{M} \in \mathbb{R}^{m\times n}$.

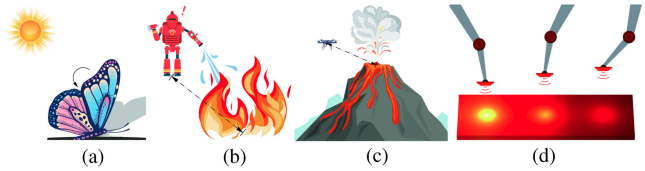

Fig. 1. Creatures and robots with thermomotor intelligence: (a) When exposed to the sun, butterflies adjust their wings configuration to control their temperature; robotic systems with thermal servoing algorithms can be used for (b) firefighting, (c) volcano exploration, and (d) industrial applications.

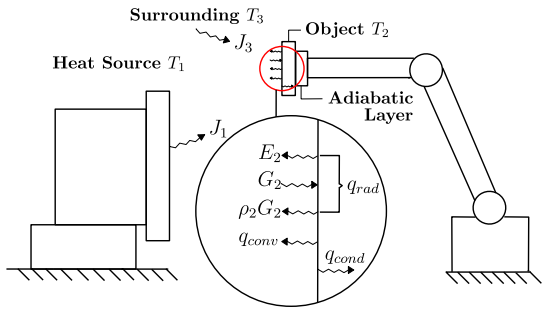

Fig. 2. Representation of the heat transfer model. A part of the object surface is magnified to show the various heat transfer processes.

In the following sections, we introduce basic thermodynamic concepts (we refer the reader to Bergman *et al.* [27] and Modest [28]) that are needed for developing the system's GTM model. To this end, consider a robot manipulator with end-effector pose denoted by $\mathbf{x} \in \mathbb{R}^n$. The robot rigidly grasps (through an adiabatic layer) a planar "small-enough" object (such that its temperature can be fairly approximated by a single sensing point), whose surface temperature is to be controlled by changing the relative pose to a heat source. The heat transfer model is composed of three main parts (depicted in Fig. 2): (i) heat source, (ii) heat collector (i.e., the object), and (iii) surrounding environment. Thermophysical parameters of different parts are denoted by the same symbol but with different subscripts. We denote the (constant) temperature of the heat source and the (varying) temperature of the object by T_1 and T_2, respectively. We assume both temperatures to be spatially uniform during the heat transfer process.[3] The environment temperature (assumed to be constant) is denoted by T_3.

Remark 1: In this article, we use the subscripts $i = 1, 2, 3$ to denote the thermophysical parameters of the heat source, the object, and the environment, respectively (a convention followed by many works dealing with heat transfer).

Heat transfer occurs amongst the three parts whenever T_1, T_2, T_3 have different values. The direction of heat transfer is always from a high temperature part to a low temperature part. We denote the net energy transfer rate to the object by Q_2, where

[3]This assumption simplifies transient heat conduction problems with the lumped capacitance method. It is generally valid for objects with high thermal conductivity, *small* characteristic length, and subject to moderate heat inflow/outflow. A quantitative valid condition of the assumption is the Biot number criterion, which is introduced in [27, Ch. 5]. For cases where the assumption is not valid, the object could be divided into different regions according to valid conditions, and multiple sensors could be used to obtain temperature feedback.

a positive value indicates energy inflow. We introduce $q_2 = Q_2/A_2$ to represent the surface's net heat flux and $v = \mathrm{d}T_2/\,\mathrm{d}t$ to describe the temporal change of the measured temperature T_2. According to the energy conservation laws, these quantities satisfy the relation

$$v = Q_2/(m_2 c_2) \tag{1}$$

where m_2 denotes object's mass and c_2 denotes the material's specific heat. To synthesize a thermal servoing controller, it is useful to find an expression of the following form:

$$v = f(\mathbf{x}, T_2) \tag{2}$$

which describes the thermal–geometric relation between the robot configuration and the temperature rate.

B. Radiation Exchange Between Planar Surfaces

In this section, we show how to calculate Q_2 between planar surfaces when thermophysical properties are known. According to different mechanisms involved in the heat transfer processes [29], the object's net heat flux q_2 satisfies the expression $q_2 = q_{\text{rad}} + q_{\text{conv}} + q_{\text{cond}}$, for radiative q_{rad}, convective q_{conv}, and conductive q_{cond} fluxes. In our case of study, thermal radiation is the dominant heat transfer mode; Note that q_{cond} and q_{conv} are negligible since the object is grasped through an adiabatic layer and the source's temperature is much higher than those of the object and environment.

Assumptions 1: We assume that the following conditions are satisfied during the task (see Fig. 2).

1) All surfaces have uniform thermophysical properties.
2) All surfaces are gray, i.e., they are diffuse emitters with equal emittance and absorptance.
3) The environment/room is modeled as a black body (i.e., $\varepsilon_3 = \alpha_3 = 1$, see the variables' definition below).

The net energy transfer rate Q_2 has the following form:

$$Q_2 = A_2 q_{\text{rad}} = A_2(\alpha_2 G_2 - E_2) \tag{3}$$

where A_2 denotes the object's surface area, G_2 the radiative flux incident at the surface, $\alpha_2 \in [0, 1]$ the object's absorptance, and E_2 the heat flux emitted by a surface (i.e., emissive power), which is approximated using the Stefan–Bolzmann law [27]

$$E_2 = \varepsilon_2 \sigma T_2^4 \tag{4}$$

with $\varepsilon_2 \in [0, 1]$ the material's emittance, and σ is the Stefan–Bolzmann constant.

Note that for an opaque surface (i.e., with zero transmittance), its reflectance ρ_i and absorptance α_i satisfy $\rho_i + \alpha_i = 1$. Radiosity is defined as $J_i = E_i + \rho_i G_i$, and since for our heat source $E_1 \gg \rho_1 G_1$, we can fairly approximate it as $J_1 \approx E_1$.

Remark 2: The view factor F_{ij} represents the fraction of J_i that is incident on surface j. The view factor depends on the end-effector configuration, i.e., $F_{ij} = F_{ij}(\mathbf{x})$. Thus, its calculation is essential for deriving the GTM model. The detailed derivation of F_{ij} for different cases and configurations is presented in later sections. Here, we assume F_{ij} is known and only focus on the derivation of Q_2.

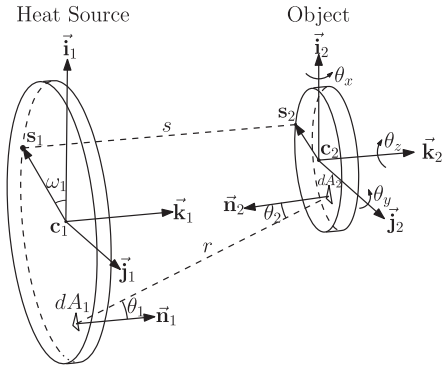

Fig. 3. Geometry of the view factor between two elementary surfaces.

The radiation incident to a surface is the summation of the corresponding portion of radiation coming from other surfaces. Thus, G_i can be calculated from the expression

$$A_2 G_2 = \sum_{j=1}^{3} F_{j2} A_j J_j = F_{12} A_1 J_1 + F_{22} A_2 J_2 + F_{32} A_3 J_3 \tag{5}$$

where by using the reciprocity relation $A_i F_{ij} = A_j F_{ji}$, the summation rule $\sum_{j=1}^{N} F_{ij} = 1$, and the planar surfaces' property $F_{ii} = 0$ (see [27]), we can simplify (5) into

$$\begin{aligned} A_2 G_2 &= F_{21} A_2 J_1 + F_{23} A_2 J_3 \\ &= F_{21} A_2 E_1 + (1 - F_{21}) A_2 E_3. \end{aligned} \tag{6}$$

Substitution of (6) into (3) yields

$$Q_2 = A_2 \alpha_2 (E_1 - E_3) F_{21} + A_2 \alpha_2 E_3 - A_2 E_2 \tag{7}$$

which we substitute alongside (4) into (1) to obtain the following key expression for the object's temperature rate:

$$v = \lambda_1 F_{21} - \lambda_2 T_2^4 + \lambda_3 \tag{8}$$

for *constant* scalar parameters λ_1, λ_2, and λ_3 satisfying

$$\lambda_1 = \frac{A_2 \alpha_2 \sigma (\varepsilon_1 T_1^4 - T_3^4)}{m_2 c_2}, \lambda_2 = \frac{A_2 \varepsilon_2 \sigma}{m_2 c_2}, \lambda_3 = \frac{A_2 \alpha_2 \sigma T_3^4}{m_2 c_2}. \tag{9}$$

C. View Factor Analytical Definition: In this section, we provide the general expression of F_{21}, which we will instantiate (in the following sections) for various configurations. To this end, consider the elementary areas $\mathrm{d}A_1$ and $\mathrm{d}A_2$ on the source and object surfaces, respectively. These areas are separated by a length r that forms polar angles θ_1 and θ_2 (see Fig. 3). The definition of the view factor is

$$F_{21} = \frac{1}{A_2} \int_{A_2} \int_{A_1} \frac{\cos\theta_2 \cos\theta_1}{\pi r^2} \,\mathrm{d}A_2 \,\mathrm{d}A_1. \tag{10}$$

The solution of (10) is usually complicated to derive. A variety of methods [30]–[33] have been proposed to calculate it. Here, we use the method in [34], which converts the double surface integrals into double contour integrals as follows:

$$F_{21} = \frac{1}{2\pi A_2} \oint_{\Gamma_1} \oint_{\Gamma_2} \ln s \,\mathrm{d}\mathbf{s}_2 \cdot \mathrm{d}\mathbf{s}_1 \tag{11}$$

where Γ_i denotes the contour of the ith surface, $\mathbf{s}_i$ the position vector of an arbitrary point on boundary Γ_i, and $s = \|\mathbf{s}_2 - \mathbf{s}_1\|$ the distance between two contour points. The advantage of using this approach is its efficient computation time [35].

D. Thermal Servoing With Parallel Circular Surfaces: In this section, we derive the thermal servoing model for two parallel source-object surfaces. To this end, we denote the surfaces' center and radius by $\mathbf{c}_i$ and r_i, respectively. The origin of the coordinate system $\vec{\mathbf{i}}_1\vec{\mathbf{j}}_1\vec{\mathbf{k}}_1$ is set at $\mathbf{c}_1$, with a unit basis vector $\vec{\mathbf{k}}_1$ along the normal $\vec{\mathbf{n}}_1$, and a unit basis vector $\vec{\mathbf{i}}_1$ perpendicular to the ground. We define $\vec{\mathbf{i}}_2\vec{\mathbf{j}}_2\vec{\mathbf{k}}_2$ as the translation of $\vec{\mathbf{i}}_1\vec{\mathbf{j}}_1\vec{\mathbf{k}}_1$, with origin at $\mathbf{c}_2$. The scalars ω_i denote the angle between $\vec{\mathbf{i}}_i$ and $\mathbf{s}_i$. We set the frames' centers at $\mathbf{c}_1 = [0, 0, 0]^\intercal$ and $\mathbf{c}_2 = [p_1, p_2, p_3]^\intercal$, with respect to $\vec{\mathbf{i}}_1\vec{\mathbf{j}}_1\vec{\mathbf{k}}_1$. The parametric position vectors $\mathbf{s}_i$ are then computed as

$$\begin{aligned}\mathbf{s}_1 &= \begin{bmatrix} r_1\cos\omega_1 & r_1\sin\omega_1 & 0\end{bmatrix}^\intercal \\ \mathbf{s}_2 &= \begin{bmatrix} r_2\cos\omega_2 + p_1 & r_2\sin\omega_2 + p_2 & p_3\end{bmatrix}^\intercal.\end{aligned} \tag{12}$$

Their differential changes satisfy the following relations:

$$\begin{aligned}\mathrm{d}\mathbf{s}_1 &= \begin{bmatrix} -r_1\sin\omega_1\,\mathrm{d}\omega_1 & r_1\cos\omega_1\,\mathrm{d}\omega_1 & 0\end{bmatrix}^\intercal \\ \mathrm{d}\mathbf{s}_2 &= \begin{bmatrix} -r_2\sin\omega_2\,\mathrm{d}\omega_2 & r_2\cos\omega_2\,\mathrm{d}\omega_2 & 0\end{bmatrix}^\intercal \\ \mathrm{d}\mathbf{s}_1 \cdot \mathrm{d}\mathbf{s}_2 &= r_1 r_2\cos(\omega_1 - \omega_2)\,\mathrm{d}\omega_1\,\mathrm{d}\omega_2.\end{aligned} \tag{13}$$

Then, the distance $s = \|\mathbf{s}_2 - \mathbf{s}_1\|$ can be derived as

$$\begin{aligned}s = s(p_1, p_2, p_3, \omega_1, \omega_2) = \big({p_1}^2 + {p_2}^2 + {p_3}^2 \\ + 2p_1(r_2\cos\omega_2 - r_1\cos\omega_1) + 2p_2(r_2\sin\omega_2 - r_1\sin\omega_1) \\ + {r_1}^2 + {r_2}^2 - 2r_1 r_2\cos(\omega_2 - \omega_1)\big)^{\frac{1}{2}}.\end{aligned} \tag{14}$$

By substituting (13) and (14) into (11), F_{21} can be calculated via

$$F_{21} = \int_0^{2\pi}\int_{2\pi}^{0} \frac{r_1 r_2}{2\pi \mathrm{A}_2}\cos(\omega_1 - \omega_2)\ln s(\mathbf{x}, \omega_1, \omega_2)\,\mathrm{d}\omega_2\,\mathrm{d}\omega_1 \tag{15}$$

where we define the end-effector position as $\mathbf{x} = [p_1, p_2, p_3]^\intercal$. By injecting (15) into (8), we can finally obtain the system's thermal–geometric relation

$$v = f(\mathbf{x}, T_2) = \lambda_1 F_{21} - \lambda_2 {T_2}^4 + \lambda_3 \tag{16}$$

where $f(\cdot)$ is the function in (2). By differentiating (16), we obtain the following key dynamic model:

$$\dot{v} = \mathbf{l}\cdot\mathbf{u} - 4\lambda_2 {T_2}^3 v \tag{17}$$

where $\mathbf{l} = \lambda_1 \frac{\partial F_{21}}{\partial \mathbf{x}}^\intercal$ denotes the interaction/Jacobian matrix (vector, in this example), and $\mathbf{u} = \dot{\mathbf{x}} \in \mathbb{R}^n$ is the robot's Cartesian velocity. The aforementioned expression is used for designing control laws for $\dot{\mathbf{x}}$ in the following sections. By using Leibniz integral rule [36], the interaction matrix can be expressed as

$$\mathbf{l} = \begin{bmatrix} \int_0^{2\pi}\int_{2\pi}^{0} h(p_1 + r_2\cos\omega_2 - r_1\cos\omega_1)\,\mathrm{d}\omega_2\,\mathrm{d}\omega_1 \\ \int_0^{2\pi}\int_{2\pi}^{0} h(p_2 + r_2\sin\omega_2 - r_1\sin\omega_1)\,\mathrm{d}\omega_2\,\mathrm{d}\omega_1 \\ \int_0^{2\pi}\int_{2\pi}^{0} h p_3\,\mathrm{d}\omega_2\,\mathrm{d}\omega_1 \end{bmatrix} \tag{18}$$

with the scalar h defined as

$$h = \lambda_1 r_1 r_2\cos(\omega_1 - \omega_2)/(2\pi A_2 s^2). \tag{19}$$

Since it is hard to analytically compute the double integrals, we use numerical methods to approximate $\mathbf{l}$ in real time.

E. Circular Surfaces in Arbitrary Configurations: In this section, we extend the parallel surfaces problem to a 6-DOF scenario, where the end-effector configuration is now defined as $\mathbf{x} = [p_1, p_2, p_3, \theta_x, \theta_y, \theta_z]^\intercal$, for θ_i as the angles around the object's coordinate system (see Fig. 3). We denote by $\mathbf{R}$ the 3-D rotation matrix corresponding to this relative orientation. Note that in some configurations of this nonparallel case, radiation from a source's region cannot reach the front side of object's surface (hence, will not contribute to the heat inflow). We refer to this problem as *self-obstruction*.

To model this situation, let us denote the object plane as $D_1 D_2 \mathbf{c}_2$, for D_1 and D_2 as the intersections with the bounded source plane. This setup is depicted in Fig. 4, where the heat source is divided into two surfaces: the red surface composed[4] of $\widehat{D_1 D_5 D_2} D_2 D_1$ and the black surface composed of $\widehat{D_2 D_6 D_1} D_1 D_2$. The black surface only "sees" the object's backside (i.e., the robot's gripper), thus, is omitted from the following calculation of F_{21}:

$$F_{21} = \frac{1}{2\pi A_2}\left(\oint_{\Gamma_a}\oint_{\Gamma_2} \ln s_a\,\mathrm{d}\mathbf{s}_2\,\mathrm{d}\mathbf{s}_a + \oint_{\Gamma_l}\oint_{\Gamma_2} \ln s_l\,\mathrm{d}\mathbf{s}_2\,\mathrm{d}\mathbf{s}_l\right) \tag{20}$$

where Γ_a denotes the arc $\widehat{D_1 D_5 D_2}$ and Γ_l the line $D_1 D_2$. To derive its respective position vectors $\mathbf{s}_a$ and $\mathbf{s}_l$, we compute the vector $\mathbf{n}_2 = [n_2^1, n_2^2, n_2^3]^\intercal$ normal to the object plane as

$$\mathbf{n}_2 = \mathbf{R}\begin{bmatrix} 0 & 0 & -1\end{bmatrix}^\intercal \tag{21}$$

whose plane equation satisfies

$$n_2^1(x - p_1) + n_2^2(y - p_2) + n_2^3(z - p_3) = 0. \tag{22}$$

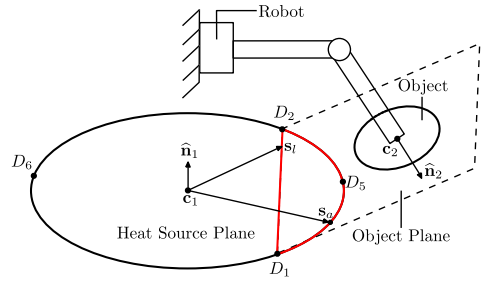

Fig. 4. Conceptual representation of a self-obstruction case.

[4]The symbol $\widehat{abc}$ denotes the arc that passes through the points a, b, and c.

To find the intersection with the plane, we use (21) and substitute $x = r_1 \cos\varphi,\ y = r_1 \sin\varphi$, and $z = 0$ into (22), for φ as a variable angle. Self-obstruction occurs when there exist two solutions φ_1 and φ_2; After some algebraic operations, the arc and line parametric vectors are obtained from

$$\mathbf{s}_a = \begin{bmatrix} r_1 \cos\varphi \\ r_1 \sin\varphi \\ 0 \end{bmatrix},\ \mathbf{s}_l = \begin{bmatrix} x_l \\ k_l(x_l - r_1\cos\varphi_2) + r_1 \sin\varphi_2 \\ 0 \end{bmatrix} \tag{23}$$

for a distance range $x_l \in [r_1 \cos\varphi_2, r_1 \cos\varphi_1]$, an angle range $\varphi \in [\varphi_1, \varphi_2]$, and a slope $k_l = \frac{\sin\varphi_2 - \sin\varphi_1}{\cos\varphi_2 - \cos\varphi_1}$ of the line D_1D_2. The parametric vector on the object's contour is computed as

$$\mathbf{s}_2 = \mathbf{R}\begin{bmatrix} r_2\cos\omega_2 & r_2\sin\omega_2 & 0 \end{bmatrix}^\intercal + \begin{bmatrix} p_1 & p_2 & p_3 \end{bmatrix}^\intercal. \tag{24}$$

As with the parallel surface case, we compute the arc and line distances $s_a = \|\mathbf{s}_2 - \mathbf{s}_a\|$ and $s_l = \|\mathbf{s}_2 - \mathbf{s}_l\|$. The 6-DOF view factor for the self-obstruction case is as follows:

$$F_{21} = \frac{1}{2\pi \mathrm{A}_2}\int_{\varphi_1}^{\varphi_2}\int_{2\pi}^{0} \ln s_a \,\mathrm{d}\omega_1 \,\mathrm{d}\varphi + \frac{1}{2\pi \mathrm{A}_2}\int_{r_1\cos\varphi_1}^{r_1\cos\varphi_2}\int_{2\pi}^{0} \ln s_l \,\mathrm{d}\omega_1 \,\mathrm{d}x_l. \tag{25}$$

With this expression, we can derive a similar GTM model $\dot{v} = \mathbf{l}\cdot\mathbf{u} - 4\lambda_2 {T_2}^3 v$, where $\mathbf{u} = \dot{\mathbf{x}} \in \mathbb{R}^6$ and the interaction matrix is $\mathbf{l} = \lambda_1 \frac{\partial F_{21}}{\partial \mathbf{x}}^\intercal \in \mathbb{R}^6$. For this 6-DOF case, we use the following *numerical* differentiation method to approximate $\mathbf{l}$:

$$\mathbf{l} = \lambda_1 \begin{bmatrix} \left(F_{21}(p_1 + \mathrm{d}p_1, p_2, \ldots, \theta_z) - F_{21}(\mathbf{x})\right)/\mathrm{d}p_1 \\ \vdots \\ \left(F_{21}(p_1, p_2, \ldots, \theta_z + \mathrm{d}\theta_z) - F_{21}(\mathbf{x})\right)/\mathrm{d}\theta_z \end{bmatrix}. \tag{26}$$

Parallel programming techniques can be applied to achieve real-time capabilities, where every element of $\mathbf{l}$ is simultaneously calculated by an independent process.

Remark 3: When the object plane and the bounded source plane do not intercept, we classify it either as a common (nonself-obstruction) case or as a complete self-obstruction case. This classification can be done by checking whether the object plane intercepts the bounded source plane. For the common case, the entire contour of the heat source will be used to calculate F_{21} (in this situation, we use (11) for calculation). For the complete self-obstruction case, we set $F_{21} = 0$.

F. Thermal Servoing Model With Multiple Objects: Here, we consider the case where the robot rigidly manipulates N "small" objects in space (for $N \leq 3$) with its end-effector, and regulates the temperature of each sensing point. The *local* range of feasible temperatures for each object is constrained by the geometry of the view factors and the rigid interobject kinematics. For this situation, we assume that heat exchange amongst the objects is negligible, therefore, the derivation of the N-object interaction matrix $\mathbf{L} \in \mathbb{R}^{N\times n}$ (where n is the number of DOF of the robot) is analogous to the previous sections and is simply constructed with N vectors $\mathbf{l}_i$ as follows:

$$\mathbf{L} = \begin{bmatrix} \mathbf{l}_1 & \cdots & \mathbf{l}_N \end{bmatrix}^\intercal. \tag{27}$$

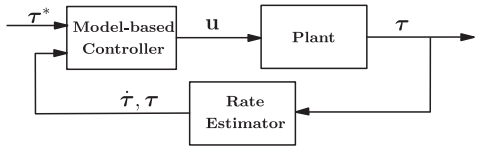

Fig. 5. Schematic representation of the model-based controller.

To effectively control each feedback temperature, the number of robot DOF must satisfy $N \leq n$. For this multiobject system, we construct the following structures:

$$\boldsymbol{\tau} = \begin{bmatrix} T_2^1 & \cdots & T_2^N \end{bmatrix}^\intercal \in \mathbb{R}^N \tag{28}$$

$$\mathbf{T} = \mathrm{diag}\left((T_2^1)^3, \ldots, (T_2^N)^3\right) \in \mathbb{R}^{N\times N} \tag{29}$$

$$\mathbf{v} = \begin{bmatrix} v^1 & \cdots & v^N \end{bmatrix}^\intercal \in \mathbb{R}^N. \tag{30}$$

The constant thermophysical parameters λ_2 are defined for ith object as λ_2^i, and are grouped into the constant matrix

$$\boldsymbol{\Lambda} = \mathrm{diag}(\lambda_2^1, \ldots, \lambda_2^N) \in \mathbb{R}^{N\times N}. \tag{31}$$

With all these terms, the GTM model can be extended to a multiobject case

$$\dot{\mathbf{v}} = \mathbf{L}\mathbf{u} - 4\mathbf{T}\boldsymbol{\Lambda}\mathbf{v}. \tag{32}$$

G. Irregularly Shaped Surfaces: In practical applications, contours are typically irregular, thus, have no simple parametric form. Depending on the requirements of the application, we can use the following two strategies to calculate the view factor (which is needed to derive the thermal interaction matrix $\mathbf{L}$): (i) If the computation power of the robot is limited (e.g., field robots), we recommend to use a simple shape (e.g., circles and rectangles) to approximate the real contour; (ii) If an accurate calculation of the view factor is required for conducting numerical simulation and analysis (as will be discussed in Section IV-F), methods such as truncated Fourier series [37] could be used to parameterize the irregular contour (we verified this approach on an Intel i7-9750H CPU using five harmonics and obtained an estimation error smaller than 0.2% with a computation time of 0.15s).

III. Controller Design

Problem statement Given a *constant* temperature reference vector $\boldsymbol{\tau}^* = [T^{*1}, \ldots, T^{*N}]^\intercal \in \mathbb{R}^N$, design a velocity-based motion controller $\mathbf{u}$ that asymptotically minimizes the feedback error $\Delta\boldsymbol{\tau} = \boldsymbol{\tau} - \boldsymbol{\tau}^*$ for all N objects.

A. Model-Based Controller

To regulate the feedback temperature of N objects,[5] we design the following velocity controller (see Fig. 5):

$$\mathbf{u} = \mathbf{L}^+(-D\mathbf{v} - K\Delta\boldsymbol{\tau} + 4\mathbf{T}\boldsymbol{\Lambda}\mathbf{v}) \tag{33}$$

[5]Throughout this article, we consider that $N \leq 3 \leq n$. The method's extension to $N > n > 3$ is straightforward (it only requires to use the left pseudoinverse). However, asymptotic stability cannot be ensured.

where $\mathbf{L}^+ = \mathbf{L}^\intercal(\mathbf{L}\mathbf{L}^\intercal)^{-1}$ is the right pseudoinverse of $\mathbf{L}$, and $D > 0$ and $K > 0$ are control gains. Note the analogy with visual servoing, which relies on the model of the first derivative of the task error, $\dot{\mathbf{e}} = \mathbf{L}\mathbf{u}$, to regulate $\mathbf{e}$ to $\mathbf{0}$ via: $\mathbf{u} = -\mathbf{L}^+ K\mathbf{e}$, which enforces the closed-loop system $\dot{\mathbf{e}} = -K\mathbf{e}$. Here, we rely on the second derivative of the task error, $\ddot{\mathbf{e}} = \mathbf{L}\mathbf{u} + \mathbf{L}'\dot{\mathbf{e}}$ (viz. system (32) with $\mathbf{e} = \Delta\boldsymbol{\tau}$, $\mathbf{v} = \dot{\mathbf{e}}$, and $\mathbf{L}' = -4\mathbf{T}\boldsymbol{\Lambda}$) and regulate $\mathbf{e}$ to $\mathbf{0}$ via: $\mathbf{u} = \mathbf{L}^+(-K\mathbf{e} - \mathbf{L}'\dot{\mathbf{e}} - D\dot{\mathbf{e}})$ [viz. controller (33)]. The closed-loop system becomes $\ddot{\mathbf{e}} = -K\mathbf{e} - D\dot{\mathbf{e}}$, which is stable, as we will show hereby.

Proposition 1: Consider that thermodynamic parameters in (32) are accurately known. For this situation, the control input (33) enforces a stable closed-loop system, which asymptotically minimizes $\|\Delta\boldsymbol{\tau}\|$.

Proof: Substituting (33) into the nonlinear dynamic system (32) yields the following closed-loop system:

$$\dot{\mathbf{v}} = -D\mathbf{v} - K\Delta\boldsymbol{\tau}. \tag{34}$$

Consider the quadratic Lyapunov function

$$\mathcal{Q}(\mathbf{v}, \Delta\boldsymbol{\tau}) = \tfrac{1}{2}\|\mathbf{v}\|^2 + \tfrac{1}{2}K\|\Delta\boldsymbol{\tau}\|^2 \tag{35}$$

whose time derivative along trajectories of (34) yields

$$\dot{\mathcal{Q}}(\mathbf{v}, \Delta\boldsymbol{\tau}) = \mathbf{v}^\intercal\dot{\mathbf{v}} + K\Delta\boldsymbol{\tau}^\intercal\mathbf{v} = -D\|\mathbf{v}\|^2 \tag{36}$$

which shows that the energy function is nonincreasing, i.e., $\dot{\mathcal{Q}} \leq 0$, thus, the closed-loop system is stable. By applying the Krasovskii–LaSalle principle, the asymptotic minimization of $\|\Delta\boldsymbol{\tau}\|$ can be proved. ■

Remark 4: In our proposed method, the terms $\mathbf{T}$ and $\boldsymbol{\tau}$ in the controller (33) can be directly obtained from real-time sensor measurements. Yet, to implement the variable $\mathbf{v}$, we use a rate estimation algorithm based on polynomial fitting with sliding windows [38].

B. Adaptive Controller

In the aforementioned model-based controller, we assume that the object's thermophysical properties are exactly known in advanced. However, due to uncertainties in the material's conditions, it is hard to know these values in practice. To deal with this issue, we propose an adaptive control strategy that does not require knowledge of the true parameters. To this end, we start by introducing the unknown parameters $a_1 = \frac{1}{\lambda_1}$ and $a_2 = \frac{\lambda_2}{\lambda_1}$, which are well-defined since $\lambda_1 > 0$; We use the superscripts a_1^i and a_2^i to distinguish them between different objects. With these parameters, we construct the following *constant* vector $\mathbf{a}_{1,2} \in \mathbb{R}^N$ and matrix $\mathbf{A}_{1,2} \in \mathbb{R}^{N\times N}$:

$$\begin{aligned} \mathbf{a}_1 &= \begin{bmatrix} a_1^1 & \cdots & a_1^N \end{bmatrix}^\intercal, \qquad \mathbf{A}_1 = \operatorname{diag}(\mathbf{a}_1) > 0 \\ \mathbf{a}_2 &= \begin{bmatrix} a_2^1 & \cdots & a_2^N \end{bmatrix}^\intercal, \qquad \mathbf{A}_2 = \operatorname{diag}(\mathbf{a}_2) > 0. \end{aligned} \tag{37}$$

By applying the dynamic expression (17) to the multiobject case and dividing it by λ_1^i for each ith object, we obtain

$$\mathbf{A}_1\dot{\mathbf{v}} + 4\mathbf{T}\mathbf{A}_2\mathbf{v} = \mathbf{J}\mathbf{u} \tag{38}$$

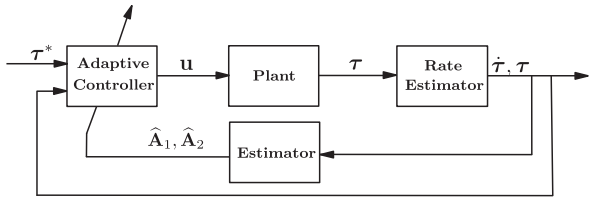

Fig. 6. Schematic representation of the adaptive controller.

for an new interaction matrix

$$\mathbf{J} = \begin{bmatrix} \mathbf{l}_1/\lambda_1^1 & \cdots & \mathbf{l}_N/\lambda_1^N \end{bmatrix}^\intercal \in \mathbb{R}^{N\times 6} \tag{39}$$

which is independent from the unknown thermophysical parameters[6] and is entirely computed with the N gradients of the view factors. To design the adaptive controller, it is useful to introduce the combined thermal error vector $\boldsymbol{\zeta} = [\zeta^1, \ldots, \zeta^N]^\intercal \in \mathbb{R}^N$ defined as

$$\boldsymbol{\zeta} = \Delta\dot{\boldsymbol{\tau}} + \mu\Delta\boldsymbol{\tau} = \mathbf{v} + \mu\Delta\boldsymbol{\tau} \tag{40}$$

for $\mu > 0$ a feedback gain. To control the N object temperatures, we design the following velocity input (see Fig. 6):

$$\mathbf{u} = \mathbf{J}^+(-\mu\widehat{\mathbf{A}}_1\mathbf{v} - K\boldsymbol{\zeta} + 4\mathbf{T}\widehat{\mathbf{A}}_2\mathbf{v}) \tag{41}$$

where the elements of the adaptive diagonal matrices $\widehat{\mathbf{A}}_i = \operatorname{diag}(\widehat{\mathbf{a}}_i) \in \mathbb{R}^{N\times N}$ are computed with the update rules

$$\dot{\widehat{\mathbf{a}}}_1 = \gamma_1\mu\begin{bmatrix} v^1\zeta^1 & \cdots & v^N\zeta^N \end{bmatrix}^\intercal \in \mathbb{R}^N \tag{42}$$

$$\dot{\widehat{\mathbf{a}}}_2 = -4\gamma_2\begin{bmatrix} v^1\zeta^1(T_2^1)^3 & \cdots & v^N\zeta^N(T_2^N)^3 \end{bmatrix}^\intercal \in \mathbb{R}^N \tag{43}$$

where scalars $\gamma_i > 0$ are used for tuning the algorithm's rate.

Proposition 2: The adaptive controller (41) with update rules (42)–(43) guarantees a bounded estimation of the unknown parameters $\mathbf{a}_1$ and $\mathbf{a}_2$, and the asymptotic minimization of the thermal error $\|\Delta\boldsymbol{\tau}\|$.

Proof: Substitution of (41) into (38) yields

$$\mathbf{A}_1\dot{\mathbf{v}} + 4\mathbf{T}\mathbf{A}_2\mathbf{v} = -\mu\widehat{\mathbf{A}}_1\mathbf{v} - K\boldsymbol{\zeta} + 4\mathbf{T}\widehat{\mathbf{A}}_2\mathbf{v}. \tag{44}$$

By adding $\mu\mathbf{A}_1\mathbf{v}$ to both sides of (44), noting that $\dot{\boldsymbol{\zeta}} = \dot{\mathbf{v}} + \mu\mathbf{v}$, and performing some algebraic operations, we can obtain

$$\mathbf{A}_1\dot{\boldsymbol{\zeta}} + K\boldsymbol{\zeta} = -\mu\widetilde{\mathbf{A}}_1\mathbf{v} + 4\mathbf{T}\widetilde{\mathbf{A}}_2\mathbf{v} \tag{45}$$

for error matrices $\widetilde{\mathbf{A}}_i = \widehat{\mathbf{A}}_i - \mathbf{A}_i = \operatorname{diag}(\widetilde{\mathbf{a}}_i)$, with error vectors $\widetilde{\mathbf{a}}_i = \widehat{\mathbf{a}}_i - \mathbf{a}_i$. To analyze the stability of the closed-loop dynamical system (42)–(43) and (45), we introduce the following Lyapunov function:

$$\mathcal{H}(\boldsymbol{\zeta}, \widetilde{\mathbf{a}}_1, \widetilde{\mathbf{a}}_2) = \frac{1}{2}\boldsymbol{\zeta}^\intercal\mathbf{A}_1\boldsymbol{\zeta} + \frac{1}{2\gamma_1}\|\widetilde{\mathbf{a}}_1\|^2 + \frac{1}{2\gamma_2}\|\widetilde{\mathbf{a}}_2\|^2 \tag{46}$$

whose time derivative along (42)–(43) and (45) yields

$$\dot{\mathcal{H}}(\boldsymbol{\zeta}, \widetilde{\mathbf{a}}_1, \widetilde{\mathbf{a}}_2) = \boldsymbol{\zeta}^\intercal\mathbf{A}_1\dot{\boldsymbol{\zeta}} + \tfrac{1}{\gamma_1}\dot{\widehat{\mathbf{a}}}_1^\intercal\widetilde{\mathbf{a}}_1 + \tfrac{1}{\gamma_2}\dot{\widehat{\mathbf{a}}}_2^\intercal\widetilde{\mathbf{a}}_2 = -K\|\boldsymbol{\zeta}\|^2 \tag{47}$$

which shows that the energy function is nonincreasing, i.e., $\dot{\mathcal{H}} \leq 0$, thus, the parameter estimation errors $\widetilde{\mathbf{a}}_i$ are bounded.

[6] An analogous result to the depth-independent interaction matrix in [39].

Asymptotic stability of $\Delta\boldsymbol{\tau}$ directly follows by applying the Krasovskii–LaSalle principle. ■

C. Target Feasibility

In previous sections, we proved that $\|\Delta\boldsymbol{\tau}\|$ can be asymptotically minimized by two automatic controllers. However, it is not guaranteed that such error can be enforced to zero. Failure cases are caused by the choice of unfeasible target temperatures: Intuitively, if targets are set to too high/low, they might be physically unachievable. In addition, for objects fixed to the same end-effector, the difference range between their target temperatures is constrained by the fixed distance between the objects. In this section, we analyze two necessary but not sufficient conditions to ensure the feasibility of the targets. Failure experiments are analyzed in Section IV-F.

Consider a simple case with two objects, object 1 and object 2, fixed to the end-effector (the extension to N object is straightforward). For one of the objects, recall the thermal–geometric relation (16) and rewrite it as follows:

$$v = -\lambda_2 {T_2}^4 + \lambda_1 F_{21}(\mathbf{x}_o) + \lambda_3 \tag{48}$$

where $\mathbf{x}_o$ denotes an object configuration. Let us assume there exists a temperature $T_2 = T_{v0}$ that makes the rate $v = 0$. As temperature is always nonnegative, T_{v0} can be solved as

$$T_{v0}(F_{21}) = ((\lambda_1 F_{21} + \lambda_3)/\lambda_2)^{\frac{1}{4}}. \tag{49}$$

Since the parameters $\lambda_i > 0$ are all positive and $F_{21} \in [0, 1)$, T_{v0} always exists. T_{v0} represents the steady-state temperature at $\mathbf{x}_o$. Note that T_{v0} is a function of F_{21} and that $\partial T_{v0}/\partial F_{21} > 0$ is always positive. Thus, the minimum value of T_{v0} is determined when $F_{21} = 0$ as

$$\min(T_{v0}) = (\lambda_3/\lambda_2)^{\frac{1}{4}} = (\alpha_2 T_3^4/\varepsilon_2)^{\frac{1}{4}}. \tag{50}$$

According to Kirchhoff's law of thermal radiation [27], at thermodynamic equilibrium, $\alpha_2 = \varepsilon_2$. Thus, the minimum is

$$\min(T_{v0}) = T_3. \tag{51}$$

When $F_{21}(\mathbf{x}_o) \to 1$, the maximum value of T_{v0} approaches

$$\max(T_{v0}) \to ((\lambda_1 + \lambda_3)/\lambda_2)^{\frac{1}{4}} = (\alpha_2 \varepsilon_1 T_1^4/\varepsilon_2)^{\frac{1}{4}} = \varepsilon_1^{\frac{1}{4}} T_1. \tag{52}$$

From (51)–(52), we derive the *first* boundary value condition

$$T^{1*}, T^{2*} \in [T_3, \varepsilon_1^{\frac{1}{4}} T_1). \tag{53}$$

Now, we discuss the limitation of the difference between target temperatures $|\delta T^*| = |T^{1*} - T^{2*}|$. We denote the configuration of the object 1 and object 2 by $\mathbf{x}_{o1} = \mathbf{x} + \Delta\mathbf{x}_1$ and $\mathbf{x}_{o2} = \mathbf{x} + \Delta\mathbf{x}_2$, respectively, where $\Delta\mathbf{x}_1$ and $\Delta\mathbf{x}_2$ are constant displacement vectors determined by the arrangement of objects. The corresponding view factors are $F_{21}(\mathbf{x}_{o1})$ and $F_{21}(\mathbf{x}_{o2})$, and steady-state temperatures are T_{v0}^1 and T_{v0}^2. From (49), $|\Delta T_{v0}| = |T_{v0}^1 - T_{v0}^2|$ can be expressed as

$$|\Delta T_{v0}(\mathbf{x}_{o1}, \mathbf{x}_{o2})| = |\chi_1(F_{21}(\mathbf{x}_{o1})) - \chi_2(F_{21}(\mathbf{x}_{o2}))| \tag{54}$$

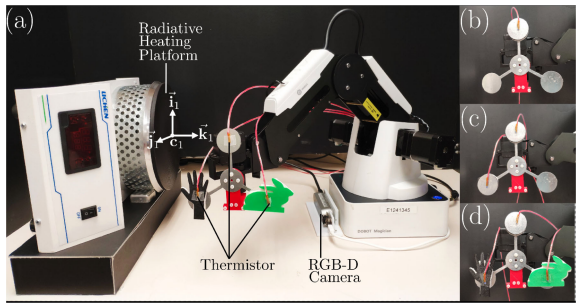

Fig. 7. Experimental setup for our radiation-based thermal servoing tests.

with functions $\chi_1(F_{21})$ and $\chi_2(F_{21})$ defined as

$$\chi_1(F_{21}) = \left(\frac{\lambda_1^1 F_{21} + \lambda_3^1}{\lambda_2^1}\right)^{\frac{1}{4}},\ \chi_2(F_{21}) = \left(\frac{\lambda_1^2 F_{21} + \lambda_3^2}{\lambda_2^2}\right)^{\frac{1}{4}} \tag{55}$$

where λ_i^1 and λ_i^2 are the thermophysical parameters of the two objects. Note that for the continuous function $\Delta T_{v0}(\mathbf{x} + \Delta\mathbf{x}_1, \mathbf{x} + \Delta\mathbf{x}_2)$, where $\mathbf{x} \in \mathbb{W}$ for $\mathbb{W}$ as the bounded workspace and $\Delta\mathbf{x}_j$ as constant vectors, there must exist a minimum value $\min(\Delta T_{v0}) = \Delta T_{v0}(\mathbf{x}^{\min})$ and a maximum value $\max(\Delta T_{v0}) = \Delta T_{v0}(\mathbf{x}^{\max})$, which encompass all possible values of ΔT_{v0}, where $\mathbf{x}^{\min}$ and $\mathbf{x}^{\max}$ are the end-effector configurations corresponding to the two extreme cases. The *second* condition for feasible target temperatures is

$$\delta T^* \in [\min(\Delta T_{v0}), \max(\Delta T_{v0})]. \tag{56}$$

A numerical (geometric) interpretation of $\mathbf{x}^{\min}$ and $\mathbf{x}^{\max}$ will be discussed in Section IV-F.

IV. Results

A. Experimental Setup

We conducted a series of experiments on a 4-DOF robot (3 translations and 1 rotation) to evaluate the proposed method. Fig. 7 shows the robot, whose end-effector is replaced by a 3-D printed connector fixed to an aluminum holder. The objects are attached to the holder through an adiabatic layer to minimize heat conduction. We prepared three different kinds of objects for temperature control experiments (see Fig. 7): An aluminum circular sheet with 1.5-cm radius and 3-mm thickness; A bunny-shaped object with 1-mm thickness, 3-D printed using polylactic acid (PLA) material with 30% infill density; A hand-shaped sheet with 1-mm thickness, also 3-D printed using PLA but with 50% infill density. We approximate the aluminum sheet's and the heat source's thermophysical properties via standard tables [27]. The object's emittance, absorptance, specific heat, and density are 0.04, 0.04, $903\,\mathrm{J}\cdot\mathrm{K}^{-1}\cdot\mathrm{Kg}^{-1}$, and $2702\,\mathrm{kg/m}^3$, respectively. The source's emittance and absorptance are estimated as 0.25 and 0.25.

For the two 3-D printed objects, different infill densities, colors, and uncertain surface conditions make their thermophysical properties hard to be estimated. Thus, we only consider the aluminum sheet for the experiments with the model-based controller (adaptive control is used for the other objects). A

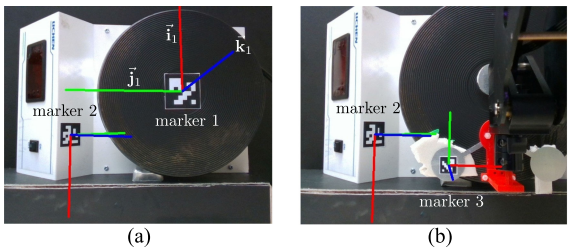

Fig. 8. Geometric calibration using ArUco markers before the experiments.

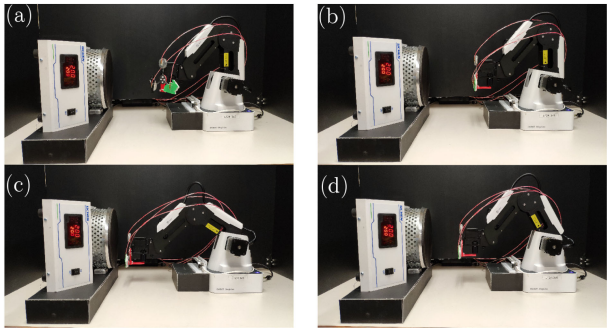

Fig. 9. Snapshots of a representative thermal servoing experiment. (a) Initial position. (b) and (c) Transient motion. (d) Steady-state configuration.

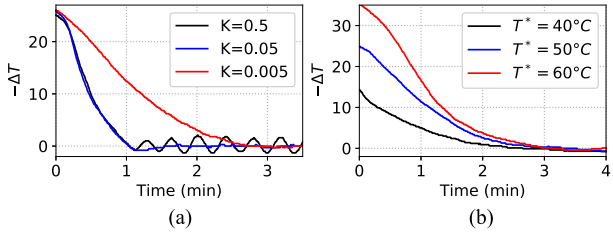

Fig. 10. Evolution ΔT of the temperature error using one aluminum object with the model-based controller.

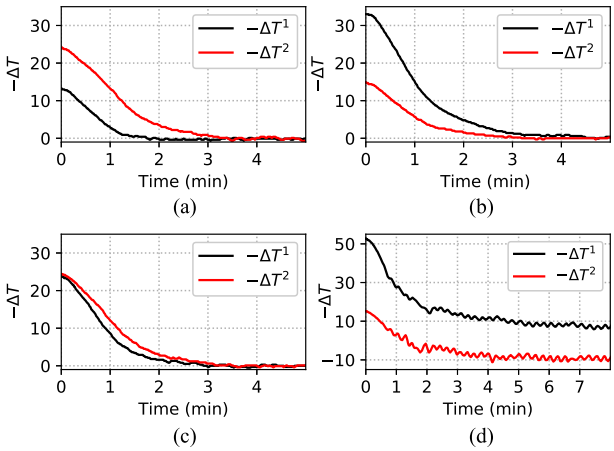

Fig. 11. Evolution of the temperature errors $(\Delta T^1, \Delta T^2)$ using two aluminum objects with the model-based controller.

radiative heating platform with adjustable temperature output is used as the heat source. The (indoor) environment temperature is assumed to be constant at 23 °C.

To obtain the feedback temperatures, we attach a PT100 platinum thermistor with 0.3 °C accuracy and 0.1 °C precision to each object. The raw data obtained by thermistors are processed by a current–temperature transformation module and sent to a Linux-based control computer as the feedback signal. The motion command is calculated by the computer program and sent to the robot under a position-stepping mode. At the beginning of the experiments, we use an RGB camera and three ArUco markers [40] to calibrate the configuration between the heat source and the end-effector (see Fig. 8).

B. Experiments With the Model-Based Controller

We conduct a series of thermal servoing experiments to evaluate our proposed control methodology (see Fig. 9 for a representative experiment). Here, we first evaluate the performance of the model-based controller with aluminum objects (whose properties are approximately known). The experiments are conducted with a source's temperature of 200 °C.

We denote the scalar temperature error by $\Delta T = T_2 - T^*$. By using the controller (33), we enforce a closed-loop heat transfer system that resembles a mass-spring-damper system. Therefore, the values of the stiffness/damping-like gains K and D can be used to specify the system's performance. Fig. 10(a) demonstrates the effect of the gain K on the thermal response. For that, we set $D = 0.2$ and $T^* = 50$ °C and conduct three experiments with different K values. These show that when $K = 0.005$ (red curve), the error ΔT asymptotically decreases to zero with a relatively slow speed; When $K = 0.05$ (blue curve), ΔT decreases faster and a small overshoot occurs; When $K = 0.5$ (black curve), ΔT oscillates near zero with an approximate 3 °C amplitude (which demonstrates the controller's capability to deal with overheating). This result shows how the closed-loop system varies from overdamped to underdamped. Thus, the gains should be specified according to the desired thermodynamic performance. We further conducted experiments with the same gains ($K = 0.05$, $D = 0.2$) but with different targets T^* and found a consistent response [see Fig. 10(b)].

Model-based experiments were also conducted to independently regulate the temperatures of two aluminum objects, as shown in Fig. 7(c). We designed four experiments with different targets $\boldsymbol{\tau}^*$ (measured in °C). Fig. 11 depicts the minimization of the thermal errors for these four experiments, with target temperatures defined as $\boldsymbol{\tau}^* = [50, 40]^\intercal$, $\boldsymbol{\tau}^* = [60, 40]^\intercal$, $\boldsymbol{\tau}^* = [50, 50]^\intercal$, and $\boldsymbol{\tau}^* = [80, 40]^\intercal$ in Fig. 11(a), (b), (c), and (d), respectively. For the first three experiments where the differences between the target temperatures $|T^{*1} - T^{*2}|$ are small (or null), the thermal error $\|\Delta\boldsymbol{\tau}\|$ can be asymptotically minimized to zero. However, when $|T^{*1} - T^{*2}|$ is large, as in Fig. 11(d), the two temperatures cannot be accurately controlled. This failure case can be explained by the second condition for feasible targets discussed in Section III-C.

C. Experiments With the Adaptive Controller

We designed a series of experiments to evaluate the performance of the proposed adaptive controller. For that, we consider

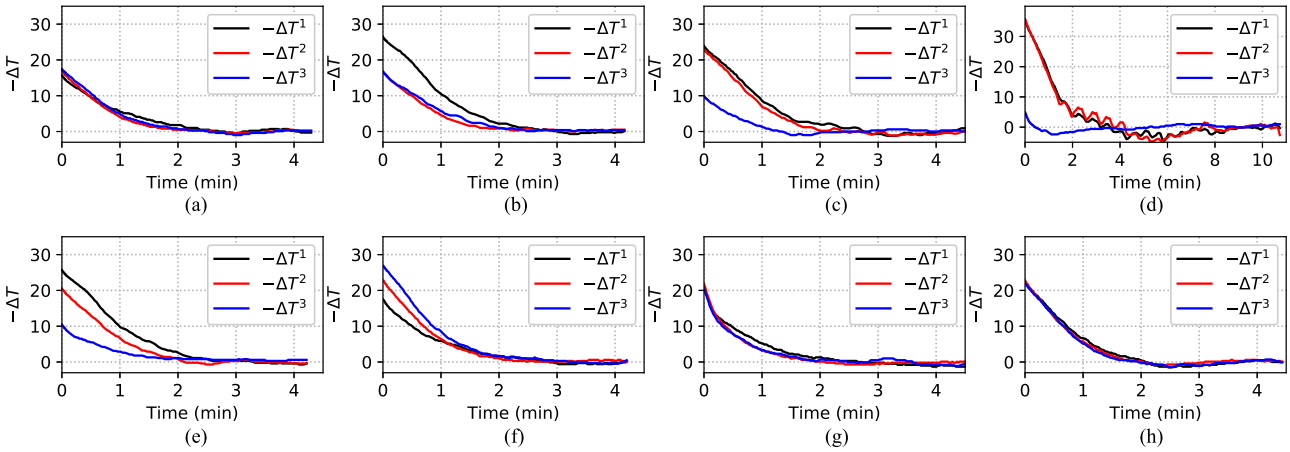

Fig. 12. Evolution of the temperature errors of the three objects in the eight experiments with the adaptive controller, ΔT^1, ΔT^2, and ΔT^3 (measured in degree Celsius). The target temperatures are set as: $\boldsymbol{\tau}^{*1} = [40 \;\; 40 \;\; 40]^\intercal$, $\boldsymbol{\tau}^{*2} = [50 \;\; 40 \;\; 40]^\intercal$, $\boldsymbol{\tau}^{*3} = [50 \;\; 50 \;\; 35]^\intercal$, $\boldsymbol{\tau}^{*4} = [60 \;\; 60 \;\; 30]^\intercal$, $\boldsymbol{\tau}^{*5} = [50 \;\; 45 \;\; 35]^\intercal$, $\boldsymbol{\tau}^{*6} = [40 \;\; 45 \;\; 50]^\intercal$, $\boldsymbol{\tau}^{*7} = [45 \;\; 45 \;\; 45]^\intercal$, and $\boldsymbol{\tau}^{*8} = [45 \;\; 45 \;\; 45]^\intercal$.

with three different objects [see Fig. 7(d)] with unknown thermophysical properties and irregular shapes. To compute the interaction matrix, we use truncated Fourier series with five harmonics terms. This approach provides a fast calculation time with a "good enough" shape approximation. The controller's gains are set to $\mu = 0.05$ and $K = 0.15$. To initialize the parameters $\widehat{\mathbf{a}}_i(0)$ at the time instance $t = 0$, we use (for the "hand" and "bunny" objects) the constant values calculated for the aluminum object in the previous model-based controller, i.e., $\widehat{\mathbf{a}}_i(0) = \mathbf{a}_i$. For the circular object, we simply initialize $\widehat{\mathbf{a}}_i(0)$ with random values.

In this study, we report eight temperature control experiments with different targets, objects, and source conditions. Fig. 12 shows the evolution of the individual thermal errors ΔT^i. For ease of presentation, we name these eight experiments as $exp1, \ldots, exp8$, and denote the corresponding target temperature for each experiment by $\boldsymbol{\tau}^{*1}, \ldots, \boldsymbol{\tau}^{*8}$. In *exp 1*, we set the three target temperatures to the same value. In *exp 2–exp 4*, we only set two targets to the same value. In *exp 5* and *exp 6*, we set all targets to different values, with a nonuniform thermal separated in *exp 5* and a uniform one in *exp 6*. In *exp 7* and *exp 8*, all targets are set to the same value, but with different heat source conditions. The source temperature T_1 is set to $200\,^\circ$C in *exp1–exp 6*, to $300\,^\circ$C in *exp7*, and varies from 200 to $300\,^\circ$C in *exp8*.

In all these experiments with all these different conditions, the magnitude of the temperature error $\|\boldsymbol{\tau}\|$ asymptotically decreases to zero. Yet, failure control experiments do happen and are reported and discussed in Section IV-F). The results experimentally confirm that (for *feasible* target temperatures) the adaptive method is able to independently regulate temperatures of various objects with different shapes and materials, without exact knowledge of their thermophysical properties or the source's/environment's temperatures.

Fig. 13 depicts the performed object trajectories during the experiments in Fig. 12. The boundary of the circular heat source is depicted as a black circle (and ellipse). The color of a trajectory point represents the feedback temperature at that position; Variation from blue to red corresponds to a change from "low" to "high." For clarity, we depict two sets of trajectory visualizations from different viewing angles: For Fig. 13 $(a_1), (b_1), \ldots, (h_1)$, the trajectories are viewed in $-\vec{\mathbf{k}}_1$ direction; For Fig. 13 $(a_2), (b_2), \ldots, (h_2)$, the trajectories are viewed in $\vec{\mathbf{i}}_1$ direction.

From these trajectory visualizations, we can see that when target temperatures are set to different values, the object with a higher target temperature usually reaches a position that is closer to the center of the heat source. This situation will be further discussed in Section IV-E. For the case when target temperatures are set to the same value, the final position of the circular aluminum sheet is always closer to the center of the heat source. This phenomenon could be explained by the fact that absorptance of a metal is usually much smaller than the absorptance of nonmetallic materials (e.g., PLA) [29]. It is also worth noting how the controller can cope with sudden changes in the source's temperature [see Fig. 12(h)].

D. Visual Recalibration of Uncertain Interaction Matrices

In this section, we report an integrated visual–thermal experiment, where the adaptive controller is combined with an online ArUco tracking algorithm to achieve temperature regulation when the source's location is uncertain. This geometric information is essential to compute the thermal interaction matrix $\mathbf{L}$.

Here, we study the case where the robot is fixed and the heat source is manually moved. We track marker 2 attached to the source to obtain its configuration. The target temperature vector is set to $\boldsymbol{\tau} = [40, 40, 40]^\intercal \;\; ^\circ$C. Fig. 14 shows: (a) The initially calibrated setup, (b) the manual movement applied to the source, (c) the detected marker 2 when the source is moving, and (d) the evolution of the individual temperature errors. These results show that by continuously updating the source-object pose, the control of the individual temperature errors is not significantly affected and that $\|\Delta\boldsymbol{\tau}\|$ can still be asymptotically minimized. This experiment demonstrates how our new thermal

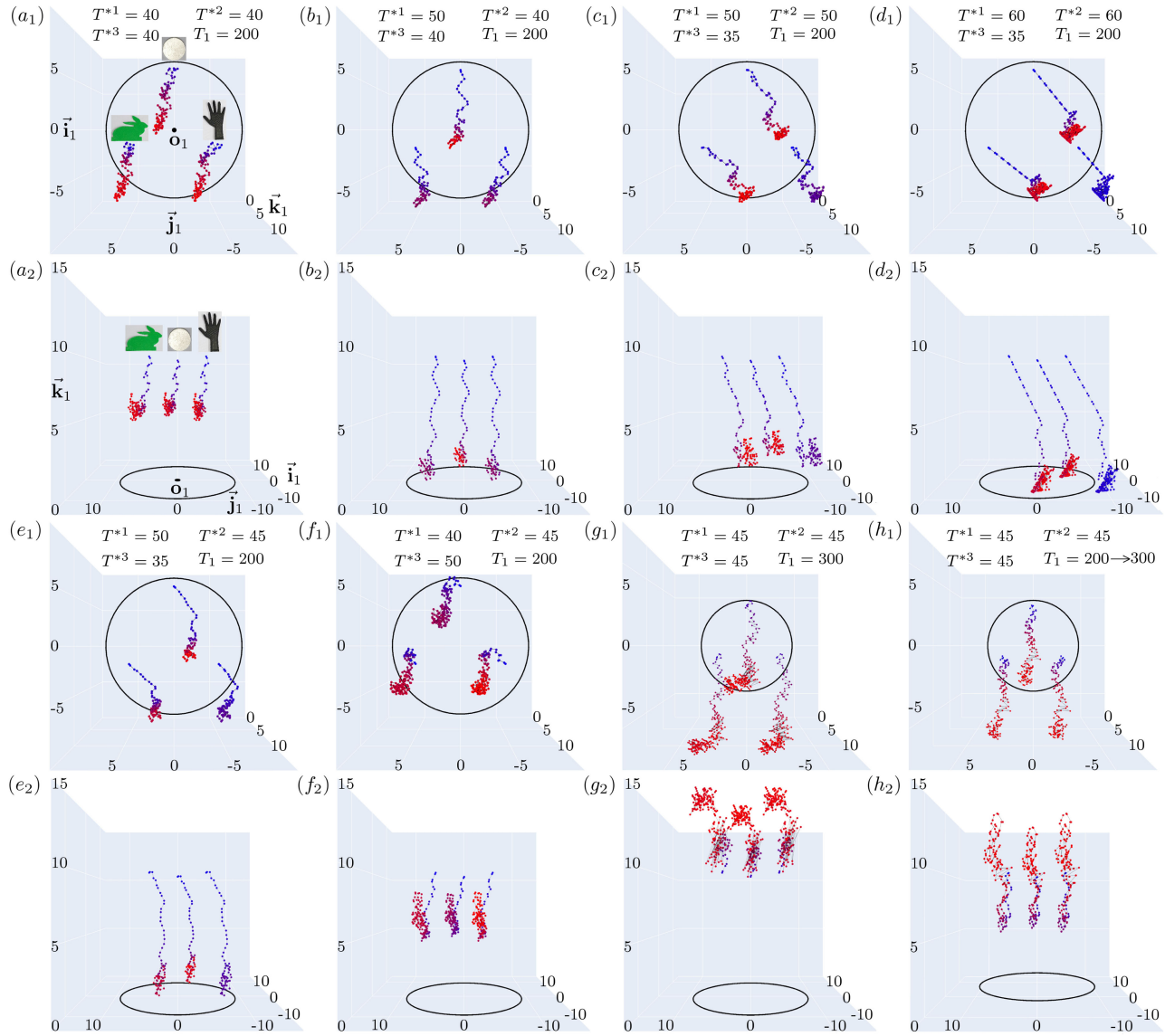

Fig. 13. Spatial displacements of the three objects in the eight experiments with the adaptive controller visualized from two viewing angles. We use a blue-to-red color gradient to visualize the cold-to-hot change of temperatures during the experiments.

servoing method can be combined with other traditional methods (vision-based controls in this case) to extend the sensorimotor capabilities of a robot [41].

E. View Factor Visualization

In previous sections, we designed thermal controllers based on derived heat transfer models. However, the models that relate F_{21} and $\mathbf{x}$ are generally complex. Therefore, part of the controlled system behaves as a "black box" to the user. To investigate these aspects, in this section, we introduce the visualization of the view factor F_{21} with respect to the end-effector configuration $\mathbf{x}$ as a useful tool for analyzing radiation-based thermal servoing problems.

As an example, we take the "circular surfaces in arbitrary configurations" case discussed in Section II-E. We implement the controlled variable method [42] to split the 6-DOF pose $\mathbf{x}$ into two subsets: One where the translation coordinates p_1, p_2, and p_3 (measured in centimeter) are the controlled variables, and another where the rotation coordinates θ_x, θ_y, and θ_z (measured in degrees) are controlled variables. In the translation subset, rotations are set to constant values of $\theta_i = 0$, then, we compute F_{21} for points in a selected working range of controlled variables $p_1, p_2 \in [-20, 20]$, $p_3 \in [0, 30]$ with a step of 1 (with 48 000 points in total). In the rotation subset, translations are similarly set to constant values $p_{1,2} = 0$ and $p_3 = 5\,\mathrm{cm}$; then, points in the range of $\theta_x, \theta_y, \theta_z \in [-90, 90]$ are computed with an incremental step of 2 (i.e., 729 000 points in total).

We use the isosurface visualization tool provided by *Plotly* [43] to visualize the data. The translation and rotations subsets are shown in Fig. 15, where 3-DOF end-effector configurations are represented by points in space, and the view factor values are

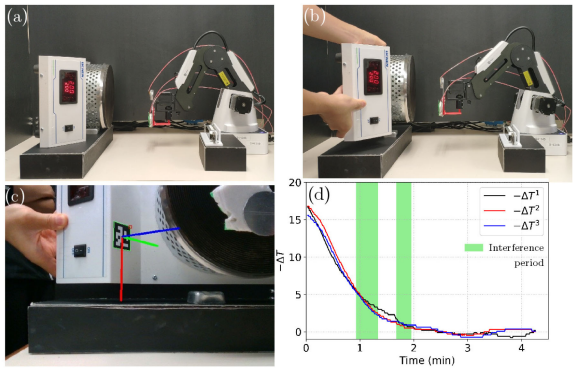

Fig. 14. Experiments with the adaptive controller with disturbances.

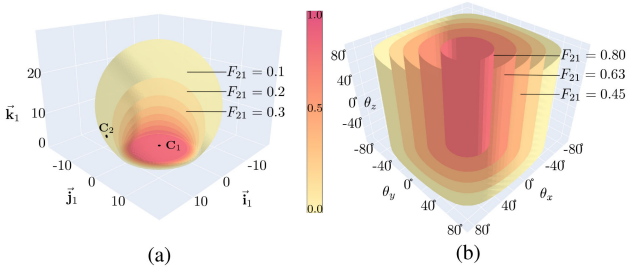

Fig. 15. Isosurface visualization of the two view factor subsets. (a) Translation subset. (b) Rotation subset.

represented by isosurfaces with different colors (the isosurfaces are formed by points that have the same or very close values of F_{21}). This visualization method is inspired by the approximation of the interaction matrix in (26), which reveals that $\mathbf{L}$ is positive proportional to the directional derivative of $F_{21}(\mathbf{x})$ along $\mathbf{x}$ as $\mathbf{L}^\intercal = \lambda_1 \nabla_{\mathbf{x}} F_{21}(\mathbf{x})$. According to the definition of isosurface, the surface normal of every point on the surface also points in $\nabla_{\mathbf{x}} F_{21}(\mathbf{x})$ direction. In addition, the interval distance between isosurfaces with an equal value difference (also called "isosurface interval") reveals the magnitudes of the elements of $\nabla_{\mathbf{x}} F_{21}(\mathbf{x})$; A larger distance represents a smaller magnitude.

As an example, let us analyze the translation subset shown in Fig. 15(a). For this single-object scenario, the normal vector at a point on the isosurface indicates the direction of the end-effector movement [as computed from the thermal controls (33) and (41)] at that point. There are some characteristics of these isosurfaces that can be intuitively deducted from the setup, e.g., the symmetric spatial distribution of F_{21} (due to the circular shape of the heat source), and the proportionality of values of F_{21} with respect to the source-object separation.

However, the visualization provides two useful pieces of information. First, that the centers of the incomplete spherical isosurfaces shift upward when F_{21} decreases, which means that at some points, movement in the $\vec{\mathbf{k}}_1$ direction will cause a decrease of F_{21} (which seems counter-intuitive). See, e.g., $\mathbf{c}_2$ on the $F_{21} = 0.1$ isosurface in Fig. 15(a), which shows that in that configuration, the end-effector needs to move backward along the $\widehat{\mathbf{k}}_1$ direction to heat up faster. Second, the isosurface intervals at regions that are farther from the heat source center are comparatively larger, which indicates that the end-effector will

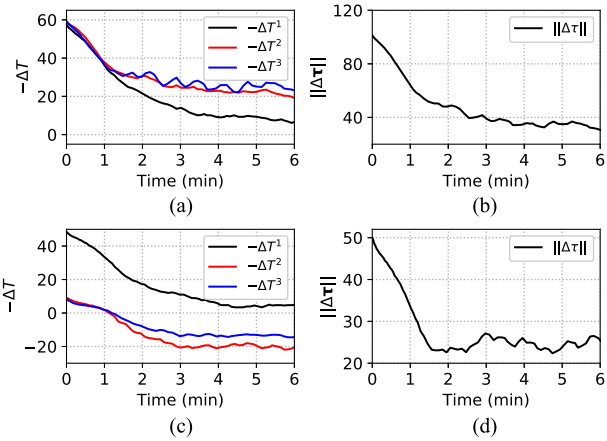

Fig. 16. Evolution of the temperature errors with unfeasible target temperatures: (top) $\boldsymbol{\tau}^* = [80, 80, 80]^\intercal$ °C, and (bottom) $\boldsymbol{\tau}^* = [70, 35, 35]^\intercal$.

move comparatively faster in those regions. Similarly, Fig. 15(b) shows the (much simpler) case where angles are varied at a fixed position.

F. Unfeasible Thermal Targets

In Section III-C, we discussed two necessary but not sufficient conditions for feasible targets. When one of the two conditions is not fulfilled, the temperature error cannot be minimized to zero. This section reports and analyzes two failed experiments with the proposed adaptive controller where the target temperatures are set to $\boldsymbol{\tau}^* = [80, 80, 80]^\intercal$ and $\boldsymbol{\tau}^* = [70, 35, 35]^\intercal$ °C. The temperature errors of each coordinate ΔT^i are depicted in Fig. 16(a) and (c). The evolution of the error $\|\Delta\boldsymbol{\tau}\|$ for the two experiments is shown in Fig. 16(b) and (d). In this experimental study, we found that when all the individual target temperatures are set relatively "high" (80 °C in this example), its corresponding errors converge to a local minimum. Also, when the difference between target temperatures is too large, one of the objects might more closely reach its target, whereas the other will present steady-state errors.

In Section III-C, we prove that the steady-state temperature of an object heated by a radiative source is directly proportional to F_{21}. Thus, the geometry of view factor isosurfaces is a useful tool for analyzing the such reachability conditions. Here, we discuss a simple but representative case where two aluminum circular sheets with radius $r_{o1} = 1.5\,\text{cm}$ and $r_{o2} = 4.5\,\text{cm}$ are attached to the end-effector at $\mathbf{o}_1$ and $\mathbf{o}_2$ (see Fig. 17) and heated by a source with $T_1 = 200\,^\circ\text{C}$. The center of the end-effector is at $\mathbf{o}_e$, and $l_{e1} = l_{e2} = 2\,\text{cm}$ are the distances between the centers $\mathbf{o}_1$ and $\mathbf{o}_2$ and the end-effector $\mathbf{o}_e$. The view factors of the objects are calculated based on the same setup as in previous sections. We use the visualization method where three translations are the controlled variables, for a parallel object and source surfaces.

By using the expression (49) and assuming that the thermophysical properties are the same, as mentioned in Section IV-A, the view factor values corresponding to steady-state temperatures 30, 40, and 50 °C are calculated as 0.12, 0.37, and 0.65. According to this one-to-one correspondence between the isosurface and the steady-state temperature, to automatically reach

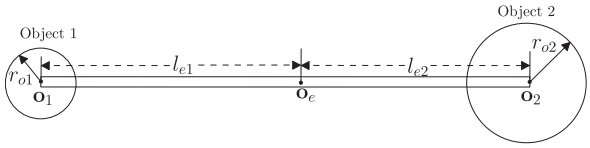

Fig. 17. Conceptual illustration of two objects fixed to an end-effector for analyzing unfeasible target temperatures.

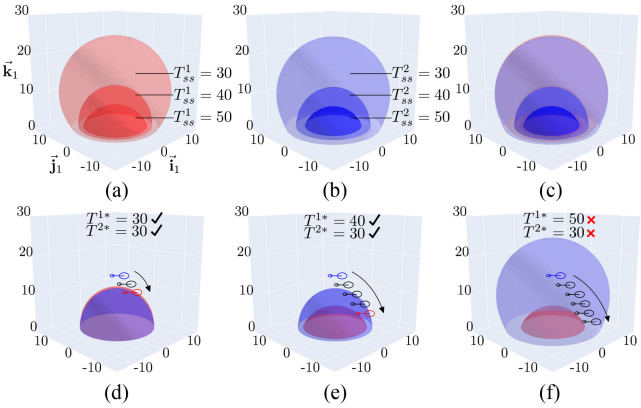

Fig. 18. Geometric explanation of the target temperature feasibility using the steady-state temperature isosurfaces. Independent control is achieved by positioning each object into its own target isosurface.

the target temperature T^* can be geometrically interpreted as positioning the object center over the isosurface that corresponds to T^*. Similarly, determining the feasibility of target temperatures T^{*1} and T^{*2} of two objects attached to the same end-effector is identical to finding whether there exists an end-effector pose that places both objects onto their "desired isosurfaces."

An example is shown in Fig. 18, where we denote the steady-state temperatures of objects 1 and 2 by T^1_{ss} and T^2_{ss}. Fig. 18(a) and (b) shows the steady-state temperature isosurfaces of objects 1 and 2 where $T^1_{\text{ss}} = T^{12}_{\text{ss}} = 30, 40, 50\,^\circ\text{C}$. Since the two objects are circular plates with different radii, the shapes of their isosurfaces are slightly different; We use red and blue color to differentiate them, and are jointly depicted in the same coordinate system in Fig. 18(c).

Fig. 18(d)–(f) depicts different combinations of target temperatures T^{1*} and T^{2*} and their corresponding isosurfaces. These figures graphically demonstrate how for thermal targets $T^{*1} = T^{*2} = 30\,^\circ\text{C}$ [depicted in Fig. 18(d)], $T^{*1} = 30\,^\circ\text{C}$, and $T^{*2} = 40\,^\circ\text{C}$ [depicted in Fig. 18(e)], the end-effector can position the objects into their desired final isosurfaces (corresponding to their target steady-state temperatures). The initial position of this trajectory is colored in blue and the final in red. However, for the case where $T^{*1} = 50\,^\circ\text{C}$ and $T^{*2} = 30\,^\circ\text{C}$, Fig. 18(f) shows that the minimum distance between the two isosurfaces is larger than $l_{e1} + l_{e2}$. Thus, targets T^{*1} and T^{*2} are *not feasible*. Similarly, if $l_{e1} + l_{e2}$ is larger than the maximum distance between two target isosurfaces, than combination of T^{*1} and T^{*2} is also unfeasible.

In addition to the aforementioned geometric explanation, we conduct an analysis of the characteristics of the entire *feasible temperature space* $\boldsymbol{\Theta}_{\text{temp}}$, which is defined as the collection of all sets of steady-state temperature $\mathbf{T}_{\text{ss}}(\mathbf{x}) = [T^1_{\text{ss}}(\mathbf{x}^1_{\text{obj}}), \ldots, T^n_{\text{ss}}(\mathbf{x}^n_{\text{obj}})]$, $\mathbf{T}_{\text{ss}}(\mathbf{x}) \in \boldsymbol{\Theta}_{\text{temp}}$ of N objects attached to the same end-effector, where $\mathbf{x}$ is the end-effector configuration, $\mathbf{x}^n_{\text{obj}}, n = 1, \ldots, N$ is the object configuration, and $T^n_{\text{ss}}(\mathbf{x}^n_{\text{obj}})$ is the steady-state temperature of an object when its center is at $\mathbf{x}^n_{\text{obj}}$. Since there is a fixed geometric relationship between $\mathbf{x}$ and $\mathbf{x}^n_{\text{obj}}$, values of $T^n_{\text{ss}}(\mathbf{x}^n_{\text{obj}})$ can be calculated according to (49).

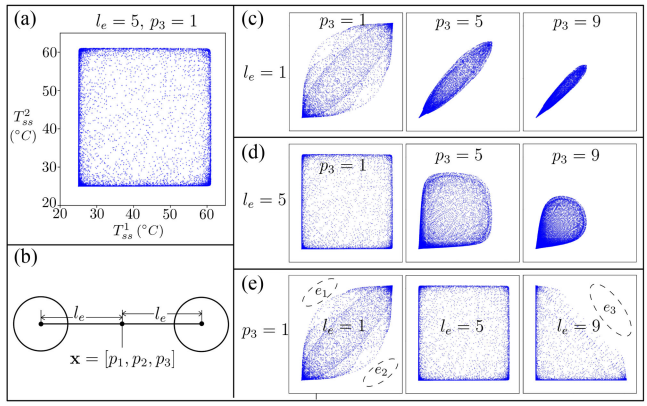

Fig. 19. Visualization of the target temperature space $\boldsymbol{\Theta}_{\text{temp}}$.

Here, we take the setup in Fig. 19(b), where two identical circular aluminium objects are attached to a 3-DOF end-effector with an identical distance l_e as a case of study. We uniformly sample a discrete end-effector configuration space where $p_1, p_2 \in [-30\,\text{cm}, 30\,\text{cm}]$, $p_3 = 1\,\text{cm}$ with a step of $0.2\,\text{cm}$ (90 000 points) and calculate the view factor values. Accordingly, $\mathbf{T}_{\text{ss}}(\mathbf{x}) \in \mathbb{R}^2$, and $\boldsymbol{\Theta}_{\text{temp}} \in \mathbb{R}^{90000\times 2}$ can be obtained. For each $\mathbf{T}_{\text{ss}}(\mathbf{x})$ in a feasible temperature space $\boldsymbol{\Theta}_{\text{temp}}$, we depict it as a 2-D point, such as in Fig. 19(a). Although $\mathbf{x}$ is uniformly sampled, the distribution of $\mathbf{T}_{\text{ss}}(\mathbf{x})$ is not uniform, which is caused by the nonlinear thermal–geometric coupling. By changing the values of l_e, p_3, several representative combinations are also depicted in Fig. 19(c)–(e). We analyze these figures and discover the following thermal–geometrical coupling characteristics.

Consider Fig. 19(c) and (d), if the end-effector moves away from the heat source (p_3 increases), the area of feasible temperature space $\boldsymbol{\Theta}_{\text{temp}}$ shrinks, which means the range of feasible temperature is smaller. However, the density of points increases; It indicates the robot motion induces a smaller change on heat transfer to the object, which to some extent increases the accuracy of temperature control when p_3 increases. Second, refer to Fig. 19(e), we discover the geometric coupling between objects (l_e in this case) also affects $\boldsymbol{\Theta}_{\text{temp}}$. If objects are close (e.g., $l_e = 1$), and the difference between the target temperature of the objects is large, these combinations of target temperature are not feasible (see the blank areas e_1 and e_2). If objects are far away (e.g., $l_e = 9$), controlling two objects to reach high temperature simultaneously is not feasible (see the blank area e_3).

For cases where $N > 3$, visualization is not practical, and some advanced data analysis is required (which is beyond the scope of this article). The analysis of the feasible temperature space reveals the physical essence of the thermal–geometric coupling, and could shed some light on practical thermal servoing system design. Nevertheless, it takes hours of computation even

with parallel-computing to obtain the required data. To quickly verify the feasibility of a specific set of target temperature, we find reformulating the problem from an optimization perspective is more effective.

Consider N objects attached to the same end-effector, the steady-state temperature of each object is denoted by $T_{\text{ss}}^n(\mathbf{x}_{\text{obj}}^n)$, $n \in \{1, 2, \ldots, N\}$. We denote the target temperature of each object by T^{n*}, then the target feasibility problem can be solved by solving the following optimization problem:

$$\min_{\mathbf{x}} \; c(\mathbf{x}) = \sum_{n=1}^{N} |T_{\text{ss}}^n(\mathbf{x}) - T^{n*}| \quad \text{s.t. } \mathbf{x} \in \mathcal{W} \tag{57}$$

where $\mathcal{W}$ is the robot working space. If the global minimum of $c(\mathbf{x})$ equals 0, the set of target temperature is feasible. We use a simple homology global optimization [44] algorithm, which is implemented in *SciPy* library, to conduct a verification of the method's feasibility. It turns out that the global minimum of $c(\mathbf{x})$ can be found effectively (in less than 1 min) for randomly selected target temperatures and geometric relationships between objects.

In general, thermophysical properties, view factors, and fixed spatial relationships between objects are the main three factors that determine the feasibility of thermal targets. The geometric interpretation of the feasibility problem might also be useful for path planninglike algorithms dealing with thermal servoing problems. The accompanying multimedia file demonstrates the performance of our method with multiple experiments, including overheat, unfeasible targets, single/multiple objects, and view factor visualizations.

V. Conclusion

In this article, we presented a new robotic temperature control technique based on heat radiation to automatically regulate temperatures of multiple objects. For that, we provided a comprehensive formulation of different scenarios of thermal servoing problems. Two asymptotically stable controllers, one model-based and one adaptive, were designed and validated by a series of experiments where temperatures of three different objects were independently regulated. We also discussed potential applications of the isosurface visualization, such as analyzing the geometry of the seemingly invisible heat transfer process.

The key concept of the proposed method was to exploit the GTM relations between the heat source and the surface for automatically computing motion controls. This advanced feedback control capability was needed to improve the performance of many economically important applications. However, from the point of view of generality, the proposed algorithm had many limitations, since we only consider cases where heat radiation was dominant. For cases where other heat transfer modes were dominant or comparable (objects in contact with nonadiabatic surfaces, electrical equipment cooled by high speed air flow, human skin treated by laser thermal excitation, food heated up in a pan, etc.), different heat transfer models need to be analyzed. Another possible solution was to implement model-free control algorithms that primarily rely on collected data instead of analytical models (which we formulated based on fundamental physical principles).

For future work, we would like to integrate thermal servoing with existing visual and proximity servoing algorithms. This multimodal perceptual and control capability is essential for developing advanced robotic temperature control systems in complex scenarios, such as service tasks in human environments and intelligent industrial manufacturing. Our team is currently working toward developing algorithms, which simultaneously consider the three basic modes of heat transfer. For this situation, *thermal images* (which provide detailed temperature profiles of an object surface) may be used as a sensing system. Sensor-based feedback control is certainly not the only way to achieve robot temperature regulation. Formulating the problem from an optimization perspective could also be interesting. For scenarios where multiple heaters attached to robots are used to heat up a large object, the coverage problem [45] in multiagent systems represents a feasible approach. The development of efficient algorithms to estimate in real time the geometry of the view factors (and hence the target's feasibility) is still an open research problem. We encourage interested readers to work along these open research directions.

References

[1] C. P. Bechlioulis, S. Heshmati-Alamdari, G. C. Karras, and K. J. Kyriakopoulos, "Robust image-based visual servoing with prescribed performance under field of view constraints," *IEEE Trans. Robot.*, vol. 35, no. 4, pp. 1063–1070, Aug. 2019.

[2] D. Navarro-Alarcon *et al.*, "Automatic 3D manipulation of soft objects by robotic arms with adaptive deformation model," *IEEE Trans. Robot.*, vol. 32, no. 2, pp. 429–441, Apr. 2016.

[3] A. Cherubini and F. Chaumette, "Visual navigation of a mobile robot with laser-based collision avoidance," *Int. J. Robot. Res.*, vol. 32, no. 2, pp. 189–205, 2013.

[4] Q. Li, O. Kroemer, Z. Su, F. F. Veiga, M. Kaboli, and H. J. Ritter, "A review of tactile information: Perception and action through touch," *IEEE Trans. Robot.*, vol. 36, no. 6, pp. 1619–1634, Dec. 2020.

[5] A. Magassouba, N. Bertin, and F. Chaumette, "Audio-based robot control from interchannel level difference and absolute sound energy," in *Proc. IEEE Int. Conf. Intell. Robots Syst.*, 2016, pp. 1992–1999.

[6] F. Rahbar, A. Marjovi, P. Kibleur, and A. Martinoli, "A 3-D bio-inspired odor source localization and its validation in realistic environmental conditions," in *Proc. IEEE/RSJ Int. Conf. Intell. Robots Syst.*, 2017, pp. 3983–3989.

[7] A. Dena, K. Ahiska, and N. Aouf, "Image based visual servoing for landmine detection using quadrotors," in *Proc. 15th IEEE Conf. Ind. Electron. Appl.*, 2020, pp. 527–532.

[8] R. Gade and T. B. Moeslund, "Thermal cameras and applications: A survey," *Mach. Vis. Appl.*, vol. 25, pp. 245–262, 2014.

[9] E. Benli, R. L. Spidalieri, and Y. Motai, "Thermal multisensor fusion for collaborative robotics," *IEEE Trans. Ind. Informat.*, vol. 15, no. 7, pp. 3784–3795, Jul. 2019.

[10] Y. Cao *et al.*, "Depth and thermal sensor fusion to enhance 3D thermographic reconstruction," *Opt. Exp.*, vol. 26, no. 7, pp. 8179–8193, Apr. 2018.

[11] Y. He and R. Yang, "Eddy current volume heating thermography and phase analysis for imaging characterization of interface delamination in CFRP," *IEEE Trans. Ind. Informat.*, vol. 11, no. 6, pp. 1287–1297, Dec. 2015.

[12] W. W.-L. Lai, K.-K. Lee, and C.-S. Poon, "Validation of size estimation of debonds in external wall's composite finishes via passive infrared thermography and a gradient algorithm," *Construction Building Mater.*, vol. 87, pp. 113–124, 2015.

[13] A. Cherubini and D. Navarro-Alarcon, "Sensor-based control for human-robot collaboration: Fundamentals, challenges and opportunities," *Frontiers Neurorobot.*, vol. 14, pp. 113–126, 2021.

[14] W. Binrui, J. Yinglian, X. Hong, and W. Ling, "Temperature control of PEM fuel cell stack application on robot using fuzzy incremental PID," in *Proc. IEEE Chin. Control Decis. Conf.*, 2009, pp. 3293–3297.

[15] M. Ho and J. P. Desai, "Towards a MRI-compatible meso-scale SMA-actuated robot using PWM control," in *Proc. IEEE Int. Conf. Biomed. Robot. Biomechatronics*, 2010, pp. 361–366.

[16] J. De Backer, G. Bolmsjö, and A.-K. Christiansson, "Temperature control of robotic friction stir welding using the thermoelectric effect," *Int. J. Adv. Manuf. Technol.*, vol. 70, pp. 375–383, 2014.
[17] J.-H. Kim and B. Y. Lattimer, "Real-time probabilistic classification of fire and smoke using thermal imagery for intelligent firefighting robot," *Fire Saf. J.*, vol. 72, pp. 40–49, 2015.
[18] A. Cammarata, "Optimized design of a large-workspace 2-DOF parallel robot for solar tracking systems," *Mech. Mach. Theory*, vol. 83, pp. 175–186, 2015.
[19] M. Muddassir, D. Gomez, L. Hu, S. Chen, and D. Navarro-Alarcon, "Robotics meets cosmetic dermatology: Development of a novel vision-guided system for skin photo-rejuvenation," *IEEE/ASME Trans. Mechatronics*, to be published, doi: 10.1109/TMECH.2021.3075207.
[20] D. McKemy, "Temperature sensing across species," *Eur. J. Physiol.*, vol. 454, pp. 777–791, 2007.
[21] J. Mlynek, R. Knobloch, and R. Srb, "Optimization of a heat radiation intensity and temperature field on the mould surface," in *Proc. 30th Eur. Conf. Model. Simul.*, 2016, pp. 425–431.
[22] A. Imdoukh, A. Shaker, A. Al-Toukhy, D. Kablaoui, and M. El-Abd, "Semi-autonomous indoor firefighting UAV," in *Proc. Int. Conf. Adv. Robot.*, 2017, pp. 310–315.
[23] G. Muscato, F. Bonaccorso, L. Cantelli, D. Longo, and C. D. Melita, "Volcanic environments: Robots for exploration and measurement," *IEEE Robot. Autom. Mag.*, vol. 19, no. 1, pp. 40–49, Mar. 2012.
[24] M. Fu, W. Weng, W. Chen, and N. Luo, "Review on modeling heat transfer and thermoregulatory responses in human body," *J. Thermal Biol.*, vol. 62, pp. 189–200, 2016.
[25] C.-C. Tsai *et al.*, "Physical and behavioral adaptations to prevent overheating of the living wings of butterflies," *Nat. Commun.*, vol. 11, no. 1, pp. 1–14, 2020.
[26] G. Arechavaleta, J. Laumond, H. Hicheur, and A. Berthoz, "An optimality principle governing human walking," *IEEE Trans. Robot.*, vol. 24, no. 1, pp. 5–14, Feb. 2008.
[27] T. L. Bergman, F. P. Incropera, D. P. DeWitt, and A. S. Lavine, *Fundamentals of Heat and Mass Transfer*. Hoboken, NJ, USA: Wiley, 2011.
[28] M. F. Modest, *Radiative Heat Transfer*. New York, NY, USA: Academic, 2013.
[29] I. Lienhard and H. John, *A Heat Transfer Textbook*. Cambridge, Massachusetts, USA: Phlogiston Press, 2005.
[30] M. Vujičić, N. Lavery, and S. Brown, "View factor calculation using the Monte Carlo method and numerical sensitivity," *Commun. Numer. Methods Eng.*, vol. 22, no. 3, pp. 197–203, 2006.
[31] J. C. Chai, J. P. Moder, and K. C. Karki, "A procedure for view factor calculation using the finite-volume method," *Numer. Heat Transfer: Part B: Fundam.*, vol. 40, no. 1, pp. 23–35, 2001.
[32] S. C. Mishra, A. Shukla, and V. Yadav, "View factor calculation in the 2-D geometries using the collapsed dimension method," *Int. Commun. Heat Mass Transfer*, vol. 35,no. 5, pp. 630–636, 2008.
[33] M. Vujičić, N. Lavery, and S. Brown, "Numerical sensitivity and view factor calculation using the Monte Carlo method," *Proc. Inst. Mech. Eng., Part C: J. Mech. Eng. Sci.*, vol. 220, no. 5, pp. 697–702, 2006.
[34] E. M. Sparrow, *Radiation Heat Transfer.* Evanston, IL, USA: Routledge, 2018.
[35] V. R. Rao and V. Sastri, "Efficient evaluation of diffuse view factors for radiation," *Int. J. Heat Mass Transfer*, vol. 39, no. 6, pp. 1281–1286, 1996.
[36] H. Flanders, "Differentiation under the integral sign," *Amer. Math. Monthly*, vol. 80, no. 6, pp. 615–627, 1973.
[37] D. Navarro-Alarcon and Y.-H. Liu, "Fourier-based shape servoing: A new feedback method to actively deform soft objects into desired 2-D image contours," *IEEE Trans. Robot.*, vol. 34, no. 1, pp. 272–279, Feb. 2018.
[38] N. Titchener, S. Colliss, and H. Babinsky, "On the calculation of boundary-layer parameters from discrete data," *Exp. Fluids*, vol. 56, no. 8, pp. 159–176, 2015.
[39] Y.-H. Liu, H. Wang, C. Wang, and K. K. Lam, "Uncalibrated visual servoing of robots using a depth-independent interaction matrix," *IEEE Trans. Robot.*, vol. 22, no. 4, pp. 804–817, Aug. 2006.
[40] S. Garrido-Jurado, R. Muñoz-Salinas, F. J. Madrid-Cuevas, and M. J. Marín-Jiménez, "Automatic generation and detection of highly reliable fiducial markers under occlusion," *Pattern Recognit.*, vol. 47, no. 6, pp. 2280–2292, 2014.
[41] D. Navarro-Alarcon, J. Qi, J. Zhu, and A. Cherubini, "A Lyapunov-stable adaptive method to approximate sensorimotor models for sensor-based control," *Frontiers Neurorobot.*, vol. 14, no. 59, pp. 1–12, 2020.
[42] C. Williams, "Research methods," *J. Bus. Econ. Res.*, vol. 5, no. 3, pp. 65–72, 2007.
[43] P. T. Inc., "Collaborative data science," Montreal, QC, Canada, 2015. [Online]. Available: https://plot.ly
[44] S. C. Endres, C. Sandrock, and W. W. Focke, "A simplicial homology algorithm for Lipschitz optimisation," *J. Global Optim.*, vol. 72, no. 2, pp. 181–217, 2018.
[45] M. Santos and M. Egerstedt, "Coverage control for multi-robot teams with heterogeneous sensing capabilities using limited communications," in *Proc. IEEE Int. Conf. Intell. Robots Syst.*, 2018, pp. 5313–5319.

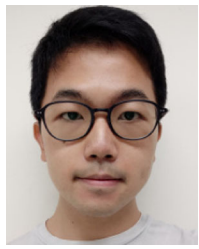

Luyin Hu received the B.Eng. degree in mechanical engineering in 2019 from The Hong Kong Polytechnic University, Hong Kong, where he is currently working toward the M.Phil. degree in mechanical engineering.

His research interests include multimodal robot perception, servomechanisms, and control system design.

David Navarro-Alarcon (Senior Member, IEEE) received the Ph.D. degree in mechanical and automation engineering from The Chinese University of Hong Kong (CUHK), Hong Kong, in 2014.

From 2015 to 2017, he was an Assistant (Research) Professor with the CUHK T Stone Robotics Institute. Since 2017, he has been with The Hong Kong Polytechnic University, Hong Kong, where he is currently an Assistant Professor with the Department of Mechanical Engineering. His current research interests include perceptual robotics and control theory.

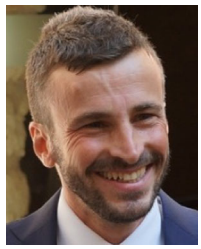

Andrea Cherubini received the M.Sc. degree in mechanical engineering from the University of Rome La Sapienza, Rome, Italy, in 2001, the second M.Sc. degree in control systems from The University of Sheffield, Sheffield, U.K., in 2003, and the Ph.D. degree in control systems from the Dipartimento di Informatica e Sistemistica, University of Rome La Sapienza, in 2008.

From 2008 to 2011, he was Postdoc with Inria Rennes, Rennes, France. Since 2011, he has been with the Université de Montpellier, Montpellier, France, first as Associate Professor, and since 2021, as Full Professor. His research interests include sensor-based control and physical human–robot interaction.

Mengying Li received the Ph.D. degree in mechanical and aerospace engineering from the University of California San Diego, San Diego, CA, USA, in 2018.

From 2018 to 2020, she was a Postdoctoral Scholar with the Center for Energy Research, UC San Diego. She joined The Hong Kong Polytechnic University, Hong Kong, as an Assistant Professor with the Department of Mechanical Engineering in 2020. Her research interests include atmospheric radiative heat transfer for renewable energy integration and design of multigeneration systems.

Lu Li received the Diploma and Ph.D. degrees in mechanical engineering from the Hefei University of Technology, Hefei, China, in 2003 and 2010, respectively.

In 2010, she joined the Hefei Institutes of Physical Science, Chinese Academy of Sciences, Hefei, as an Assistant Research Fellow and became an Associate Research Fellow in 2015. Her research interests include design and control of robotic systems, legged robots, and human–machine interactive systems.